



# 1 Marine snow surface production and bathypelagic export at the 2 Equatorial Atlantic from an imaging float

3 Joelle Habib<sup>1</sup>, Lars Stemmann<sup>1,6</sup>, Alexandre Accardo<sup>1</sup>, Alberto Baudena<sup>1</sup>, Franz Philip Tuchen<sup>2,3</sup>, Peter Brandt<sup>4,5</sup>,  
4 Rainer Kiko<sup>1,4,5</sup>

5 <sup>1</sup>Sorbonne Université, CNRS, Laboratoire d'Océanographie de Villefranche, LOV, 06230 Villefranche-sur-Mer,  
6 France

7 <sup>2</sup>Cooperative Institute for Marine and Atmospheric Studies, Rosenstiel School of Marine, Atmospheric, and Earth  
8 Science, University of Miami, Miami, FL, USA

9 <sup>3</sup>NOAA/Atlantic Oceanographic and Meteorological Laboratory, Miami, FL, USA

10 <sup>4</sup>GEOMAR Helmholtz Centre for Ocean Research Kiel, Kiel, Germany

11 <sup>5</sup>Faculty of Mathematics and Natural Sciences, Kiel University, Kiel, Germany

12 <sup>6</sup>Institut Universitaire de France (IUF), Paris, France

13 *Correspondence to:* Joelle Habib (joellehabib22@hotmail.com)

14 **Abstract.** The marine biological carbon pump (BCP) plays a central role in the global carbon cycle, transporting  
15 carbon from the surface to the deep ocean and sequestering it for long periods. Sinking of surface-produced  
16 particles, known as the Biological Gravity Pump (BGP) constitutes the main component of the BCP. To study the  
17 BGP in the equatorial Atlantic upwelling region, a biogeochemical (BGC) Argo float equipped with an Underwater  
18 Vision Profiler 6 (UVP6) camera was deployed from July 2021 to March 2022. The float was recovered after its  
19 eastward drift from 23°W to 7°W along the equator, during which it conducted profiles to 2000 m depth every  
20 three days. For the first time in this oceanic region, in situ images and physical and biogeochemical data from a  
21 BGC-Argo float were acquired and analyzed in combination with satellite data. During the float trajectory, two  
22 blooms were recorded followed by two main export events of sinking aggregates that lasted for over a month,  
23 consistently reaching 2000 m depth. A Lagrangian approach was applied to investigate the production,  
24 transformation, and deep export of marine particles. Based on the characterization of the morphology of detritus  
25 within and outside of the plumes, five particle morphotypes with different sinking properties were detected. Small  
26 and dense aggregates were present throughout the water column while porous morphotypes, despite being larger,  
27 were predominantly concentrated in the surface layer. Export was driven by small and compact particles with higher  
28 particle abundance and flux during upwelling and export events. Our investigation reveals the stability of the  
29 equatorial Atlantic BCP system during this period, yielding an export efficiency of 6-7% during and outside of  
30 export events. This study highlights the importance of using new technologies on autonomous platforms to  
31 characterize the temporal variability in the magnitude and functioning of the BCP.

## 32 1 Introduction

33 The term “biological carbon pump” (BCP) encompasses physical and biological processes responsible for the  
34 generation, export, and remineralization of organic matter from the upper ocean to depth (Boyd et al., 2019;  
35 DeVries et al., 2012; Steinberg & Landry, 2017). The biological pump connects various aspects of the carbon cycle:  
36 the upper-ocean photosynthetic carbon uptake, the alimentation of the midwater biota (Irigoiien et al., 2014), and  
37 the carbon storage within the deep sea (Buesseler et al., 2007). Within the euphotic zone, organic particles are  
38 continuously generated and recycled, with only a small fraction descending into deeper layers (De La Rocha, 2004),  
39 while remineralization occurs within a few hundred meters of the surface and is facilitated by processes such as



40 zooplankton feeding or microbial degradation (Giering et al., 2014; Steinberg & Landry, 2017; Stemmann, Jackson,  
41 & Ianson, 2004). Given the retroactive potential of the BCP to significantly impact anthropogenic climate warming  
42 (Bernardello et al., 2014; Bopp et al., 2013), understanding the multitude of mechanisms governing the BCP is of  
43 paramount importance.

44 Among the different processes of the BCP, sinking marine snow is the key component of particulate carbon  
45 transport to the deep ocean, a process known as the biological gravitational pump (BGP). Marine snow consists of  
46 detritus, formed from a mixture of source particles produced by the surface ecosystem and aggregated together by  
47 physical (coagulation) or biological (trophic activity) mechanisms (Alldredge & Silver, 1988). Their composition  
48 is determined by multiple characteristics, mainly the phytoplankton and zooplankton community composition  
49 (Bach et al., 2019; Tréguer et al., 2018). In the mesopelagic layers, several biological and physical factors influence  
50 their dynamics and control their size distribution and morphology, which affect their sinking (Cael et al., 2021;  
51 Stemmann, Jackson, & Ianson, 2004). Shear and differential settling modulates aggregation (Jackson, 1990;  
52 Stemmann et al., 2004) while fragmentation rates have been proposed to depend on shear and swimming organisms  
53 (Briggs et al., 2011; Dilling & Alldredge, 2000; Jackson, 1990). Additionally, particle volume and surface area  
54 condition interactions with microorganisms (e.g., colonization and degradation of particles; Bianchi et al., 2018),  
55 modifying marine snow morphology by making them more porous and fragile with time (Biddanda & Pomeroy,  
56 1988; Ploug & Grossart, 2000).

57 An efficient tool to track the particle morphology, study their abundance, and estimate the vertical carbon flux is  
58 the Underwater Vision Profiler (UVP; Picheral et al., 2010, 2022). This imaging tool measures particle abundance  
59 and distribution (Guidi et al., 2009; Kiko et al., 2022; Stemmann et al., 2002), to estimate the biological  
60 gravitational pump (Forest et al., 2013; Guidi et al., 2015; Kiko et al., 2017; Ramondenc et al., 2016), and more  
61 recently, to explore particle morphology (Trudnowska et al., 2021; Accardo et al., submitted). One decade of  
62 observation with the UVP5 during ship surveys allowed a global monitoring (Forest et al., 2013; Guidi et al., 2008,  
63 2015; Kiko et al., 2017; Stemmann et al., 2002) and enabled the reconstruction of global export fluxes from the  
64 spatially variable euphotic zone and mixed layer depths (Clements et al., 2022, 2023; Guidi et al., 2015).

65 Despite significant improvement in observation capacities from ships, high frequency observations during long-  
66 term deployment to study relevant scales of marine snow dynamics over a large depth range was not possible.  
67 Autonomous platforms equipped with imaging sensors have emerged and are currently being utilized to remotely  
68 record plankton and particle distributions in addition to the core parameters such as salinity, temperature, and  
69 optically derived other variables (Claustre et al., 2020; Picheral et al., 2022). Recently, surface blooms followed  
70 by plumes of sinking material were monitored using optical sensors (fluorescence and backscatter) mounted on  
71 BGC-Argo float drifting in a quasi-Lagrangian mode (Briggs et al., 2011, 2020) and global POC standing stocks  
72 have been calculated (Fox et al., 2024). Such studies with optical sensors (fluorescence, backscatter) are key to  
73 understanding particle dynamics in the core of the oceans but they are not adapted to study marine snow.

74 We selected the equatorial Atlantic Ocean to conduct our study, as it is characterized by enhanced primary  
75 productivity concentrated within the equatorial and coastal regions (Grotsky et al., 2008). This productivity is due  
76 to the presence of upwelling zones in the central and eastern parts of the equatorial basin (Schott et al., 1998) which  
77 bring nutrients to the euphotic zone (Radenac et al., 2020). This enhanced productivity results in a stronger passive



78 and active export of particulate matter reaching up to 4000 m (Kiko et al., 2017). The strength of the equatorial  
79 upwelling system is modulated by the strength of seasonally varying winds associated with the meridional  
80 migration of the intertropical convergence zone (Brandt et al., 2023). At intraseasonal (20-50 days) scales, Tropical  
81 Instability Waves (TIWs) are another factor influencing the equatorial local productivity. TIWs are westward-  
82 propagating, cusp-shaped oscillations prevalent in the central and western equatorial Atlantic generated by  
83 baroclinic and barotropic instabilities (Athie & Marin, 2008). They induce strong intraseasonal variations in sea  
84 surface temperature, sea surface salinity, and ocean currents (Tuchen et al., 2022), and are associated with sharp  
85 fronts (Warner et al., 2018). TIWs can also influence nitrate (Radenac et al., 2020) and chlorophyll distribution  
86 (Menkes et al., 2002; Sherman et al., 2022).

87 We here focus on the equatorial Atlantic BGP, using data from a UVP6 camera mounted on a BGC-Argo float  
88 deployed at 23°W, 0° in July 2021 to study the impact of seasonal upwelling and intraseasonal TIWs on  
89 productivity and particle export. In particular, we use a plume-based approach to follow the initiation and vertical  
90 extent of export events, to characterize particle production of various morphotypes during two bloom events, and  
91 to describe the patterns of their attenuation as they are exported to the meso- and bathypelagic layers.

## 92 **2 Material and Methods**

### 93 **2.1 Satellite data**

#### 94 **2.1.1 Sea surface chlorophyll-a**

95 Estimates of chlorophyll-a (chl-a) concentration and anomalies for the tropical Atlantic were obtained from the  
96 combination of two different products: the Global Ocean Color product  
97 (OCEANCOLOUR\_GLO\_BGC\_L4\_MY\_009\_104) produced by ACRI-ST and the NOAA-VIIRS provided by  
98 NOAA CoastWatch. Both of these data sets provide gap-free time series, with a temporal extent from 1997 till  
99 2023 for the first product, while the second one only started in 2018. The temporal resolution for both products is  
100 one day with a spatial resolution of 4 km for the first product and 9 km for the second one.

#### 101 **2.1.2 Sea surface temperature**

102 Sea surface temperature (SST) and SST anomaly data were downloaded from the NOAA OI-SST data set (Huang  
103 et al., 2021; <https://psl.noaa.gov/data/gridded/data.noaa.oisst.v2.highres.htm>). SST anomalies are computed  
104 relative to a 30-year climatological mean. The gridded data are available daily from 1981-present at a horizontal  
105 resolution of 0.25°. To isolate TIW induced SST variability from the time series, a temporal (20-50 days) and a  
106 zonal (4-20° wavelength) bandpass filter were applied in accordance with previous studies (Olivier et al., 2020;  
107 Tuchen et al., 2022).

#### 108 **2.1.3 Lagrangian diagnostics**

109 Several Lagrangian diagnostics were computed for each sampling station using velocity data and environmental  
110 satellite products. To this aim, we defined for each station a circular region that we consider representative of the  
111 water parcel sampled by the BGC-Argo float. A radius of 0.1° was used (consistently with previous studies,  
112 Baudena et al., 2021; Fabri-Ruiz et al., 2023; Ser-Giacomi et al., 2021), and the circular region was filled with  
113 virtual particles. A given diagnostic is calculated for each virtual particle in the circular region. These values are  
114 then averaged together, providing one value of a given diagnostic per station.



115 The velocity field used is the Copernicus CMEMS product MULTIOBS GLO PHY REP 015 004-TDS at 15 m  
116 depth. This product has a spatial resolution of  $0.25^\circ$  and a daily temporal resolution. It is derived from satellite  
117 altimetry and model assimilation and includes both geostrophic and Ekman components. Using the surface velocity,  
118 each particle within the circular region of a given sampling station was advected using a Runge-Kutta scheme of  
119 order 4 from the day of the sampling backward in time. Different advective times were used, from 5 to 45 days.  
120 Two types of diagnostics were carried out: Eulerian and purely Lagrangian diagnostics. These groups consist of  
121 calculating properties that are integrated in time: at the sampling location (Eulerian) or along the trajectory of the  
122 water parcel (Lagrangian). In this study, we only present diagnostics that are relevant to our area of study, such as  
123 the Lagrangian and Eulerian chl-a, divergence, and vorticity. The Lagrangian chlorophyll, the average chl-a content  
124 carried by the water parcel in the previous days, provides information on the recent primary productivity. The  
125 Lagrangian divergence can be considered as a proxy of the upwelling (when negative) of downwelling (when  
126 positive) experience by the water parcel in the previous days. This metric has been correlated with chlorophyll  
127 (Hernández-Carrasco et al., 2018).

128 In the following, we will report diagnostics calculated using an advective time of 15 days. This value was chosen  
129 as it showed the highest correlations between the chl-a concentrations and the abundance of micrometric particles  
130 and macroscopic particles between 0-100m (Supplementary Fig. S8).

## 131 **2.2 Float data**

### 132 **2.2.1 Coverage and data collection**

133 For this study, a BGC-Argo float (WMO:6904139) was deployed at the equator during *RV Sonne* SO284 cruise  
134 traversing the transect from  $23^\circ\text{W}$  to  $7^\circ\text{W}$  migrating from west to east during the period between July 2021 and  
135 March 2022. The float was recovered during the PIRATA FR32 cruise. This float was equipped with several  
136 physical and biogeochemical sensors to measure the pressure, temperature, salinity, chlorophyll, oxygen, and  
137 particle backscattering coefficient (BBP) with a vertical resolution of 5 m. BGC-Argo float data were collected  
138 through the International Argo Program and can be found at <https://argo.ucsd.edu>. Chl-a and BBP both present a  
139 gap between the 1<sup>st</sup> and the 5<sup>th</sup> of January 2022.

### 140 **2.2.2 UVP measurements**

141 An Underwater Vision Profiler 6 (UVP6) was mounted on the BGC Argo float. This camera-based particle counter  
142 sizes and counts marine particles (Kiko et al., 2022) covering a size range from 0.102 mm to 16.4 mm. The UVP  
143 contributes to understanding sinking organic particles and carbon sequestration at global (Guidi et al., 2015) and  
144 regional scales (Ramondenc et al., 2016). More information about calibration and data processing can be found in  
145 Picheral et al. (2021). In total, our data set includes 86 profiles reaching at least 1000 m. Every 3 days, the BGC  
146 Argo float reached 2000 m. For all parameters, we interpolated the data set with a vertical resolution of 10 m and  
147 a temporal resolution of a day.

### 148 **2.2.3 Mixed layer depth calculation**

149 To determine the mixed layer depth, we use temperature profiles provided by the BGC-Argo float. Using the  
150 definition outlined in De Boyer Montégut et al. (2004), the mixed layer was determined by identifying the depth at



151 which the temperature decreased by 0.2°C relative to the temperature at 10 m depth. The mixed layer depth in this  
152 study reached a depth of 60 m.

#### 153 **2.2.4 Particle abundance and carbon flux calculation**

154 Particle size abundances (number of particles per liter) for depth bins of 2.5 m along the water column were  
155 obtained by the UVP. Particles were divided into two categories based on their size: Micrometric particles (MiP)  
156 for particles ranging between 0.1-0.5 mm, and Macroscopic particles (MaP) ranging between 0.5-16 mm. The  
157 carbon flux was obtained by integrating all size classes and therefore represents the total carbon flux. To calculate  
158 the flux for a given size class, we used the relationship provided by Kriest (2002), linking the particle size to the  
159 sinking speed and its carbon content. This relationship has been used in former studies using UVP observations  
160 (Kiko et al., 2017). For each parameter, we interpolated the profiles in depth with a vertical resolution of 10 m and  
161 a temporal resolution of a day.

#### 162 **2.2.5 Determination of export events**

163 We determined periods of export events, using the anomalous carbon flux. We calculated the total mean particle  
164 abundance and mean carbon flux along the water column from the interpolated fields for the deployment period.  
165 The resulting mean profile was then subtracted from the individual particle abundance and carbon flux profiles,  
166 yielding anomaly profiles. This helped us determine two different types of periods: periods with main export events  
167 and periods where no or weak export occurred.

#### 168 **2.2.6 Regime shift detection for surface export**

169 A sequential algorithm for regime shift detection (Rodionov, 2004) was applied to the MaP abundance for the first  
170 200 m to identify accurately the beginning and the end of the carbon export events. This method identifies  
171 discontinuities in a time series without prior assumptions of the timing of the regime shifts. The algorithm requires  
172 a set of parameters to specify: the target significance level and the cutoff length. The target significance used here  
173 is  $p=0.05$ . The cutoff length affects the time scale of the regime by removing regimes of shorter duration than the  
174 reference value. In this study, the cutoff length was set to 9 days to cover at least 3 profiles. For more details, see  
175 Rodionov (2004, 2006). We determined three masks, two corresponding to periods of export ‘event 1’, ‘event 2’,  
176 and a period where no main export plume was observed, hereafter referred to as the ‘outside-between’ mask. It  
177 should be noted that ‘outside-between’ refers to periods that do not belong to the two main export events.

#### 178 **2.2.7 Morphological properties of detritus**

179 The data set consisted of 127,000 images. Each image underwent individual classification using the Ecotaxa  
180 program with the support of machine learning classifiers (Picheral et al., 2017). This classification differentiates  
181 between living and non-living organisms. The automatically classified images were then manually validated or  
182 reclassified. To distinguish between different types of marine snow, we examined the morphological properties of  
183 individual objects such as size (area, perimeter), shade intensity (mean/median gray level), shape (elongation), and  
184 structural complexity (homogeneity or heterogeneity of gray levels). This was done using a principal component  
185 analysis (Fig. S6) to summarize the morphological information into a few new variables, followed by k-means  
186 clustering to separate different morphotypes of particles (Trudnowska et al. 2021). Using this method, we  
187 distinguish between five types of marine snow, as this number was a good compromise between the continuum of



188 change in morphology and a need for simplicity. Concentration in numbers (numbers m<sup>-3</sup>) was computed per 10 m  
189 bins for each UVP6 profile.

## 190 **2.2.8 Flux attenuation and biological carbon pump efficiency**

191 The biological carbon pump (BCP) was computed following Engel et al. (2023), and Buesseler et al. (2020):

$$192 \quad BCP = E_{eff} \times T_{eff} \quad (1)$$

193 With  $E_{eff}$ , as the carbon export efficiency ( $E_{eff}$ )

$$194 \quad E_{eff} = \frac{F_{Z0}}{PP} \quad (2)$$

195  $F_{Z0}$  is the carbon export flux out of the surface ocean layer, corresponding to 100 m. While PP is the amount of  
196 CO<sub>2</sub> fixed by primary production, both in mg m<sup>-3</sup> d<sup>-1</sup>. Satellite-based net primary production (NPP) was  
197 downloaded from the Ocean Productivity website ([www.science.oregonstate.edu/ocean.productivity](http://www.science.oregonstate.edu/ocean.productivity)) using the  
198 Vertically Generalized Production Model (VGPM)-Eppley.

199  $T_{eff}$  represents the carbon transfer efficiency:

$$200 \quad T_{eff} = \frac{F_Z}{F_{Z0}} \quad (3)$$

201  $F_Z$  is the flux at a particular depth and  $Z_0$  is the reference depth (taken here as 100 m).  $T_{eff}$  is related to the attenuation  
202 of carbon flux with depth, over 0-1000 m, quantified by a Martin power law (Martin et al., 1987).

$$203 \quad F_Z = F_{Z0} \times \left(\frac{Z}{Z_0}\right)^{-b} \quad (4)$$

204  $Z$  is the depth. The exponent  $b$  represents the attenuation with depth. An analogous equation was used to describe  
205 the particle attenuation.

$$206 \quad n_Z = n_{Z0} \times \left(\frac{Z}{Z_0}\right)^{-b} \quad (5)$$

207  $n_Z$ ,  $n_{Z0}$  are the concentrations of particles at depth  $Z$  or  $Z_0$ .

## 208 **3 Results**

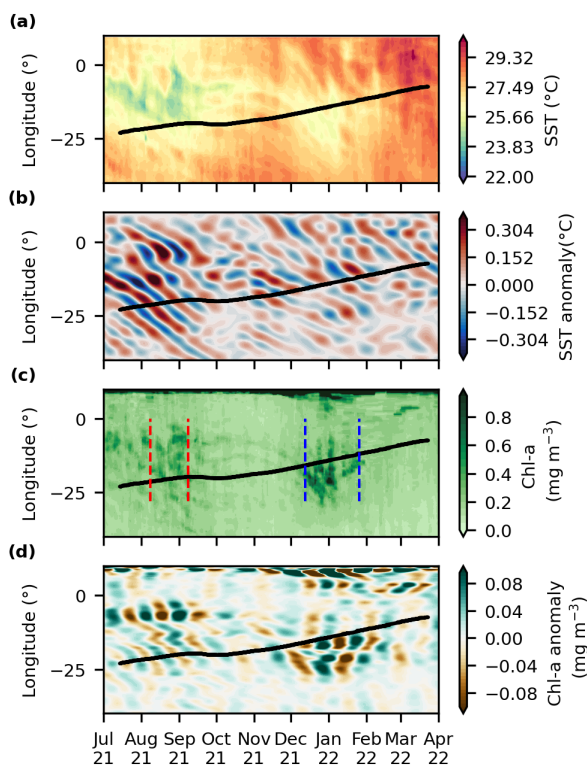
### 209 **3.1 Satellite data analysis**

210 Throughout the float trajectory (Fig. S1), satellite observations disclosed the presence of relatively cold surface  
211 waters during two distinct periods: August-October 2021 and December 2021 to February 2022 (Fig. 1a). The first  
212 period aligned with the seasonal development and peak of the Atlantic cold tongue with minimum surface  
213 temperatures around 23.8°C. The second period was from December to February with temperatures around 26°C.  
214 The seasonal surface warming occurring between October and December featured values reaching 27.5°C, while  
215 temperatures reached almost 29.5 during March and April (Fig. S2a). The temperatures were warmer than usual  
216 compared to the climatology from 2012-2022, especially throughout the boreal summer of 2021 (Fig. S2a).



217 Before and during the cold tongue development in July to September 2021, bandpass-filtered SST anomalies  
218 oscillated between  $-0.3^{\circ}\text{C}$  and  $0.3^{\circ}\text{C}$  and showed westward propagation (Fig. 1b), suggesting the presence of TIWs.  
219 A weaker TIW signal was observed during the second period when SST anomalies ranged between  $-0.1^{\circ}\text{C}$  and  
220  $0.1^{\circ}\text{C}$ .

221 Peaks of chl-a were observed during both low-temperature periods reaching about  $0.4\text{ mg m}^{-3}$  on 10 September  
222 2021 and 2 January 2022 (Fig. 1c, S2b). The surface chl-a concentration ranged between  $0.1$  and  $0.4\text{ mg m}^{-3}$  along  
223 the float trajectory. When comparing the chl-a to the climatology, a delay in both peaks was observed (Fig. S2b)  
224 with a low peak during summer 2021 and a second high peak during winter 2022 for the float compared to the  
225 climatology. The bandpass-filtered chl-a anomaly oscillated between  $-0.04\text{ mg m}^{-3}$  and  $0.04\text{ mg m}^{-3}$  from August  
226 to October (Fig. 1d). These anomalies seem to be anti-correlated with the SST anomalies (Fig. S2 c,d). However,  
227 westward propagation of bandpass-filtered chl-a anomalies is less obvious than for SST. From December to March,  
228 more pronounced chl-a anomalies were observed.



229

230 **Figure 1: Satellite-derived properties as a function of time (x-axis) and longitude (y-axis): (a) sea surface temperature**  
231 **(°C), (b) bandpass-filtered sea surface temperature anomaly, (c) surface chl-a concentration ( $\text{mg m}^{-3}$ ), and (d) bandpass-**  
232 **filtered chl-a anomaly along the equator from July 2021 to March 2022. The black line represents the float trajectory**  
233 **from west to east. The blue and red lines determine the beginning and the end of the first and the second export event,**  
234 **respectively.**



## 235 **3.2 Float data analysis**

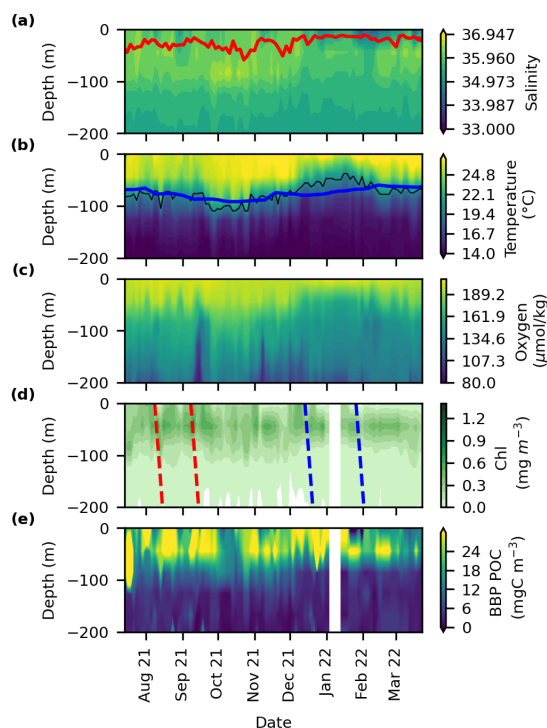
### 236 **3.2.1 Physical parameters (Temperature, Salinity, mixed layer)**

237 During August, the mixed layer depth (MLD) was at about 42 m, salinity integrated over the first 100 m showed a  
238 maxima of 36 PSU (Fig. 2a, S3a) while temperature (averaged over the top 100 m) showed a first minimum of  
239 21°C (Fig. 2b). Average 100-m temperature increased with the progressive deepening of the ML from September  
240 to January. MLD reached a maximum of 60 m in October. Salinity was high during the same period with a  
241 maximum of 36 psu in November (Fig. 2a). A second 100-me temperature minimum of 18.8°C was also recorded  
242 in January coinciding with the shoaling of the Deep Chlorophyll Maximum (DCM) and the presence of a salinity  
243 minimum in the top 100 m (Fig 2a,b, S3a,b). A subsurface maximum was determined for the salinity between 50-  
244 100 m (Fig. 2a,b). The thermocline, represented by the 20°C isotherm (black line, Fig. 2,e) was unusually deep  
245 during summer (80 m) compared to the Argo climatology and reached a maximum of 100 m in October. It was  
246 also unusually shallow (50 m) in January 2022.

### 247 **3.2.2 Biogeochemical parameters (chl-a, BBP, oxygen)**

248 The chl-a concentration reported by the BGC-Argo float in the first 100 m, varied between 0 and 0.5 mg m<sup>-3</sup>. Peaks  
249 reached 0.45-5 mg m<sup>-3</sup> values on September 18, November 3, and 8 December (Fig. 2d, S3a). Elevated chl-a  
250 concentrations were observed at 70 m depth, corresponding to the depth of the deep chl-a maximum. These values  
251 varied between 0.28 and 0.8 mg m<sup>-3</sup>. Both satellite and float chl-a data show the presence of two blooms (Fig. S3a).  
252 However, float data presented a more variable chl-a concentration compared to the satellite. This can be attributed  
253 to the low resolution of satellite images compared to the float and the interpolation methods applied to ensure a  
254 gap-free time series. BBP POC, calculated using a BBP-to-carbon relationship (Koestner et al., 2022), followed  
255 the same pattern as chl-a and small particles were concentrated in the first 90 m (Fig. 2e). Periods of high chl-a  
256 were correlated with an increase in the BBP POC. Oxygen concentrations reached values around 189 μmol kg<sup>-1</sup>  
257 (Fig. 2c) in the mixed layer. Concentrations decreased with depth, with values below 134 μmol kg<sup>-1</sup> below 100 m.





258  
259 **Figure 2: Time–depth profiles determined from the BGC-Argo float for (a) salinity, (b) temperature (°C), (c) oxygen**  
260 **( $\mu\text{mol kg}^{-1}$ ), (d) chl-a ( $\text{mg m}^{-3}$ ) (e) and BBP POC ( $\text{mgC m}^{-3}$ ). The red line in (a) represents the mixed layer depth defined**  
261 **as a decrease of  $0.2^\circ\text{C}$  relative to temperature at 10 m depth. The black line in (b) represents the  $20^\circ\text{C}$  isotherm depth**  
262 **which is a well-known proxy for the thermocline in the tropics. The blue line in (b) is the average depth of the  $20^\circ\text{C}$**   
263 **isotherm from the Argo climatology (2012 to 2022). The blue and red dashed lines in (d) determine the beginning and**  
264 **the end of the first and the second export event, respectively.**

### 265 3.3 Carbon flux dynamics

#### 266 3.3.1 Surface flux and particle abundance along the trajectory (0–100m)

267 The increase in surface chl-a in the first 100 m was linked to an increase in surface carbon flux and MiP abundance  
268 (particles between 0.1–0.5 mm) (Fig. S3). Both were significantly correlated with in situ chl-a ( $r^2=0.4$  and  $0.3$ ,  
269 respectively,  $p\text{-value}<0.01$ ). No significant correlation was found between surface chl-a and MaP abundance  
270 (particles $>0.5$  mm). The highest integrated MiP abundance in the surface layer was recorded on the 18<sup>th</sup> of August  
271 2021 with values reaching  $316 \text{ particles L}^{-1}$  (Fig. 3a,c, S3d). This also coincided with the highest MaP abundance  
272 with around  $5 \text{ particles L}^{-1}$ . Simultaneously with the surface chl-a peak, on 3 November 2021 a peak of MiP with  
273  $348 \text{ particles L}^{-1}$  was also observed (Fig S3d), while carbon flux increased after a 15 day delay reaching  $250 \text{ mg C}$   
274  $\text{m}^{-2} \text{ day}^{-1}$  (Fig. S3f). The peak of chl-a, in December 2021 caused an increase in carbon flux, MiP, and MaP  
275 abundance.

#### 276 3.3.2 Flux and particle abundance pattern along the water column (averaged profile)

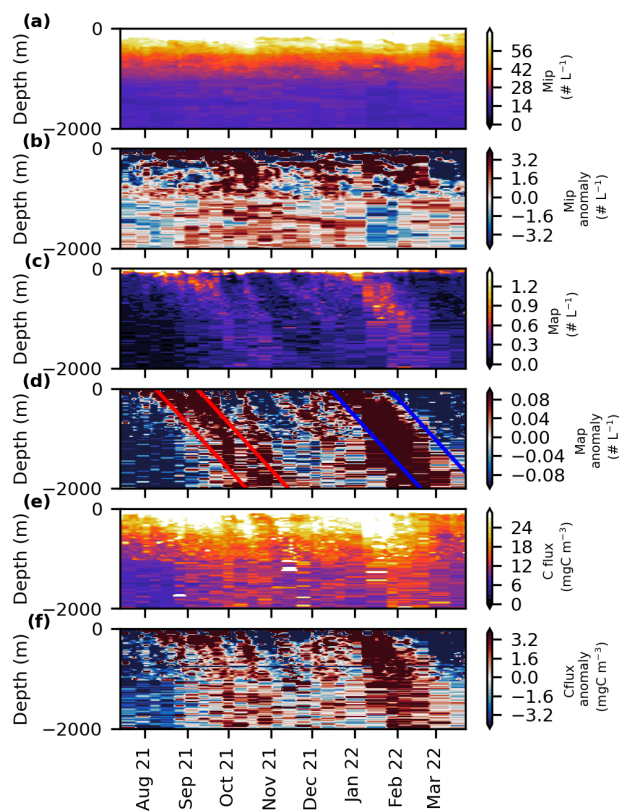
277 Throughout the float trajectory, the UVP6 data showcased high variability in MiP and MaP abundance, and carbon  
278 flux in the upper 100 m, with a dominance of small particles compared to big particles (Fig. 4a, S3). MiP and MaP  
279 increased in the surface layer peaking at 30–40 m, respectively. The maximum carbon flux,  $104.1 \pm 61.5 \text{ mgC m}^{-3}$



280 day<sup>-1</sup>, coincided with the MaP's maximum. After the surface layer peaks, MiP abundance and carbon flux declined  
281 rapidly until 1000 m, reaching  $22.5 \pm 1.3$  particles L<sup>-1</sup> and  $13.2 \pm 2.9$  mgC m<sup>-3</sup> day<sup>-1</sup>, while MaP's abundance  
282 decreased rapidly until 200 m with  $0.3 \pm 0.2$  particles L<sup>-1</sup>. Flux and abundance declined further with depth. The  
283 carbon flux was dominated by MiP abundance and followed its pattern.

### 284 3.3.3 Evaluation of export events

285 To investigate two settling plumes depicted in Figure 3d, four spaced lines were drawn on the MaP abundance with  
286 a slope of 30 m day<sup>-1</sup>, as suggested by Stemmann, Jackson, & Gorsky, (2004) using a model for particle size  
287 distribution. The periods of surface production and export were determined using the Rodionov algorithm (Fig.  
288 S4). The first export event, "Event 1", started at the surface on the 8th of August and lasted until the 8th of  
289 September 2021, while the second event, "Event 2", occurred from the 13th of December 2021 to the 26th of  
290 January 2022. Both events lasted one month (Fig. 3f). These events are easily discernible on the MaP abundance  
291 and carbon flux plots as two plumes that reach 2000 m depth (Fig. 3c-f) while they are less visible in the MiP  
292 pattern.

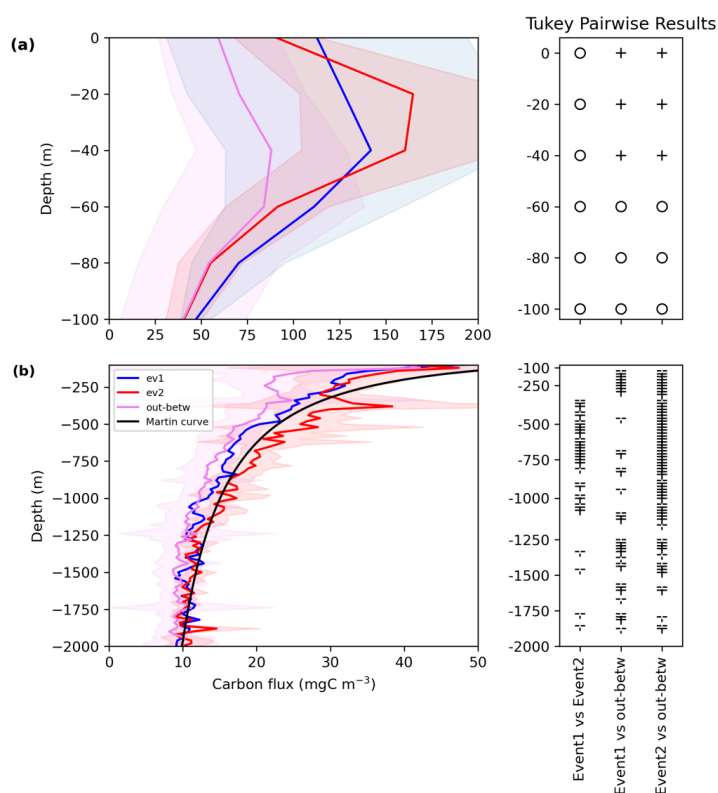


293

294 **Figure 3: Time series of (a) MiP abundance (# L<sup>-1</sup>), (b) MiP anomaly, (c) MaP abundance (# L<sup>-1</sup>), (d) MaP anomaly, (e)**  
295 **carbon flux (mgC m<sup>-3</sup> day<sup>-1</sup>), and (f) carbon flux anomaly. The blue and red lines determine the beginning and the end**  
296 **of the first and the second export event, respectively.**



297 Interestingly, the carbon flux profiles for events 1 and 2, and the ‘outside-between’ mask showed the same  
 298 attenuation of the mean carbon flux along the water column (Fig. 4a,b). Flux at 30 m depth reached 168, 139, and  
 299 83  $\text{mg C m}^{-3} \text{ day}^{-1}$  for event 2, 1 and outside-between mask, respectively (Fig. 4a). The flux then decreased with  
 300 depth during all periods. An intermediate particle maximum was observed for ‘outside-between’ and event 2  
 301 between 300-500 m (Fig. S5). The ‘outside-between’ mask showed the lowest carbon flux along the water column  
 302 compared to the two export events. Flux during event 2 was the highest from 0-60 m and then from 120 m to 2000  
 303 m (Fig. 4a-c). Post hoc Tukey tests showed a significant difference between the outside-between mask and the two  
 304 main export events for most of the layers of the water column (Fig. 4), while there was rarely a difference between  
 305 events 1 and 2.



306

307 **Figure 4:** Averaged carbon flux profiles ( $\text{mg C m}^{-3}$ ) along the plumes during event 1 (blue), event 2 (red), and the outside-  
 308 between mask (purple) (a) from 0-100 m, (b) from 200-2000 m. The shading represents the standard deviation. The  
 309 Tukey pairwise results were conducted for each depth. Plus signs indicate a significant difference, and blank space or  
 310 empty circles indicate a non-significant difference. The black line represents the Martin curve of event 2 calculated using  
 311 Eq. 4 with  $b=-0.6$  and  $F_{z0}=100\text{m}$ .

### 312 3.3.4 Flux attenuation and export efficiency

313 We parameterize the strength of the BCP pump using the export efficiency calculated at 100 m. Export efficiency  
 314 ranged between 6-7% of the NPP (from satellite data estimates) exiting the 0-100 m layer. The attenuation rate of  
 315 carbon flux was determined using a power law regression fit. The b values ranged between -0.4 and -0.6. The best



316 transfer efficiency was found during event 2, where 40% of the flux at 100m reaches 1000m, followed by the  
317 between-outside mask and event 1 (31% and 29%, respectively; Table 1).

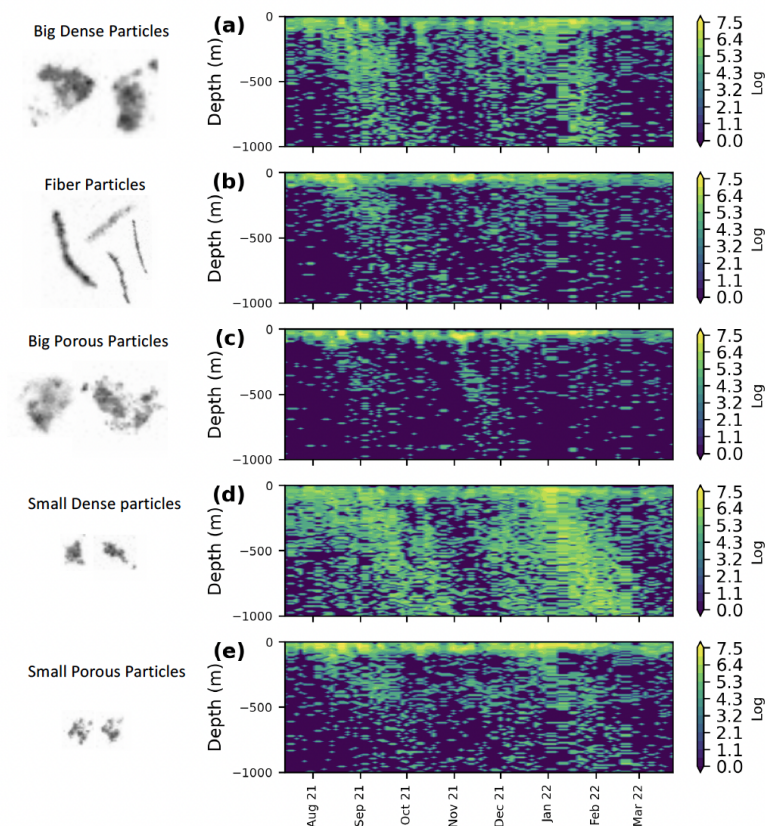
318 **Table 1: Parameters characterizing the biological carbon pump efficiency calculated in the plumes**

	Outside-between mask	event 1	event 2
$E_{\text{eff}}$	7%	7%	6%
$T_{\text{eff}}$	31%	29%	40%
b	-0.48	-0.53	-0.6

### 319 **3.4 Particle composition**

#### 320 **3.4.1 Morphotypes of marine snow and composition of the different events**

321 The k-means clustering applied to the PCA coordinates helped us to distinguish between five marine snow  
322 morphotypes illustrated in Figure 5. Type 1 consisted of big and dense objects (Big Dense Particles, BDP) with an  
323 Equivalent Spherical Diameter (ESD) $>0.8\text{mm}$ . Type 2 comprised elongated objects (Fiber particles: FP), and type  
324 3 consisted of big, bright, and porous objects (Big Porous particles: BPP). Type 4 was mainly formed of dense,  
325 small, and circular objects (Small Dense particles: SDP) and type 5 consisted of light grey, small, and porous  
326 objects (Small Porous particles: SPP). These five morphotypes were then used to characterize the distribution and  
327 composition of marine snow. It should be noted that the terms "porous" and "dense" refer to brightness, with  
328 "porous" indicating greater light transmission.



329

330 **Figure 5: Time series of the logarithmic concentration of (a) Big Dense, (b) Fiber, (c) Big Porous, (d) Small Dense, and**  
331 **(e) Small Porous morphotypes.**

332 The different detritus morphotypes showed high concentrations of particles in the surface, especially during the  
333 export events (Fig. 5, S7). They shared similar temporal dynamics primarily in the surface layer: FP, BPP, BDP,  
334 SDP, and SPP decreased exponentially between 0 and 150 m. While FB, BPP and SPP decreased slowly throughout  
335 the water column in the mesopelagic layers, BDP and SDP increased gradually between 400-600 m and then  
336 decreased again (Fig. S7). BDP and SDP presented two discernable plumes during the two delineated export events,  
337 reaching 2000 m with significant concentrations all along the plumes (Fig. 6a,d, S6). Other morphotypes such as  
338 FP and SPP were sometimes present in deeper layers but with low concentrations. In the deeper mesopelagic, only  
339 SDP showed no decrease with depth (Fig. S7).

340 SPP were most abundant across the different periods (Fig. S7). For the outside-between mask, these particles  
341 constituted 28% within the 0-100 m range. In events 1 and 2, their presence increased up to 50-60% within the 0-  
342 50 m range (Fig. S7). However, this percentage notably declined between 50-100 m for events 1 and 2 with values  
343 dropping to 25% below 100 m. It further decreased between 100-150 m outside of these events, 18% below 150 m  
344 (Fig. S7). BPP and FP also exhibited high concentrations within the upper 100 m where they were primarily located.



345 Even though BDP and SDP were the least preponderant classes in the first 100 m, they dominated deeper layers  
346 compared to clusters BPP, SPP, and FP which were found almost exclusively in the surface layer. Their proportions  
347 were more than 20% for events 1 and 2 and 15% outside of these export events in the first 100 m. Concentrations  
348 of small, dark, and compact marine snow decreased until 200 m and then increased until 1000 m, while big, dark,  
349 and compact particles decreased until 400-450 m for all masks and increased afterward (Fig. S7). Small compact  
350 particles showed a mean proportion of more than 40% for both events and 28% for the period outside of those (Fig  
351 S7). Throughout the observation period, the vertical attenuation of dark, compact, and small particles was the  
352 lowest of all marine snow categories with visibly more dark dense morphotypes in deep waters for all periods,  
353 while the highest vertical attenuation amongst all marine snow types was observed for the BPP cluster.

### 354 **3.5 Lagrangian diagnostics**

355 To determine the optimal advective time scale for the different particle sizes, we correlated both MiP and MaP  
356 abundance in the first 100 m with the Lagrangian chl-a (chlorophyll in the moving water mass) for the different  
357 advective times (from 0-45 days). The highest correlation was determined for  $t=15$  days (Fig. S8). Chl-a and BBP  
358 POC were positively correlated with MiP in the first 100 m (Fig. S9). While MaP showed a low correlation with  
359 chl-a. As for the different morphotypes, FP, SDP, and SPP were significantly correlated with chl-a while no  
360 significant correlation was observed with BDP and BPP. POC flux, MiP, and MaP abundances were also  
361 significantly correlated with the Lagrangian vorticity and divergence for an advective time scale of 15 days.

## 362 **4. Discussion**

### 363 **4.1 Cold tongue and TIW related equatorial upwelling dynamics**

364 The equatorial Atlantic follows a pronounced seasonal cycle in upwelling activity, forced by the seasonal winds  
365 and the meridional migration of the intertropical convergence zone (Brandt et al., 2023), which translates into a  
366 respective cycle of productivity (Grotsky et al. 2008) and a slight seasonality in carbon export (Fischer et al., 2000;  
367 Wefer & Fischer, 1993).

368 Here, we use a combination of satellite data analysis and in situ biogeochemical and image-based measurements  
369 from a BGC-Argo / UVP float to further our understanding of equatorial Atlantic biological pump dynamics. We  
370 observed relatively cool SST between August and October corresponding to the occurrence of the Atlantic Cold  
371 Tongue (ACT; Brandt et al., 2011), and during boreal winter in December and February corresponding to a  
372 secondary cooling period as was reported by Jouanno et al. (2011) and Okumura & Xie (2006). Seasonal cooling  
373 events are largely linked to diapycnal heat flux out of the mixed layer into the deeper ocean (Hummels et al., 2013).  
374 This heat flux is due to the enhancement of the vertical shear driven by the strength and the direction of the surface  
375 current (Jouanno et al., 2011) and the eastward Equatorial Undercurrent (EUC) at the thermocline level (Hummels  
376 et al., 2013). The equatorial Atlantic was warmer than usual at the surface throughout the boreal summer of 2021.  
377 This was the result of the occurrence of a strong Atlantic Niño driven by wind and equatorial wave forcings (Lee  
378 et al., 2023; Song et al., 2023; Tuchen et al., 2024). The physical processes controlling the downward heat flux out  
379 of the mixed layer also control the upward supply of nitrate to the euphotic layer (Radenac et al., 2020). The  
380 equatorial Atlantic is a nitrate-limited upwelling regime (Grotsky et al., 2008; Moore et al., 2013) and modeling  
381 studies showed that in the equatorial Atlantic, the seasonal variations in chl-a are closely linked to the seasonal  
382 variability of the nitrate input via upwelling and mixing (Loukos & Mémery, 1999; Radenac et al., 2020). The chl-



383 a blooms that are normally found in the equatorial Atlantic are linked to the upwelling of nitrate-rich thermocline  
384 waters during these periods and the diffusive flux of nitrate into the mixed layer through mixing (Longhurst, 1993;  
385 Radenac et al., 2020). Likewise, we found that chl-a concentration followed a pronounced semiannual cycle with  
386 peaks in boreal summer and winter, as also described by Grodsky et al. (2008) and Brandt et al. (2023). During the  
387 first peak, from August to October, the thermocline was relatively deep compared to climatology (as a consequence  
388 of the presence of the Atlantic Niño), and chl-a levels were likewise relatively low. A shallower nitracline together  
389 with a shallower EUC (Tuchen et al., 2024) during the second peak in boreal winter might have favored the growth  
390 of the phytoplankton assemblage showing anomalously high chl-a levels. These variations with respect to the  
391 climatological cycle are in agreement with what was proposed by Grodsky et al. (2008) that the interannual  
392 variability of the secondary bloom in boreal winter is as large as those of the primary bloom in boreal summer,  
393 even though its climatological expression is weaker.

394 Another process affecting local productivity at the equator is intraseasonal TIWs with a 20-50 days period range  
395 as indicated by the bandpass-filtered SST and chl-a anomalies. In this study, elevated primary production was  
396 located between 10°W-25°W in a region affected by TIWs. Their occurrence strongly suggests that TIWs might  
397 influence the biogeochemistry of the equatorial upper-ocean system. On the one hand, TIWs are associated with  
398 meridional currents at the equator modulating the boundary of the Atlantic cold tongue eventually resulting in local  
399 variations of SST and chl-a. On the other hand, TIWs are associated with phases of enhanced mixing (Foltz et al.,  
400 2020; Heukamp et al., 2022; Inoue et al., 2019; Moum et al., 2009) or front generation (Warner et al., 2018) leading  
401 to upward nutrient supply. It has been suggested that TIWs could enhance upper-ocean fertilization by promoting  
402 local nitrate upwelling alleviating the nitrate depletion which usually affects this region (Radenac et al., 2020;  
403 Sherman et al., 2022). Enhanced chlorophyll concentration has been associated with TIWs suggesting that TIWs  
404 drive intraseasonal chl-a variability (Grodsky et al., 2008; Menkes et al., 2002; Shi & Wang, 2021). Pronounced  
405 positive and negative anomalies in bandpass-filtered chl-a data were anti-correlated with anomalies in bandpass-  
406 filtered positive SST anomalies. The SST anomalies were moderate during the secondary bloom in boreal winter,  
407 accompanied by a shallower thermocline. However, during that period, a pronounced chl-a bloom was observed  
408 together with the largest bandpass-filtered chl-a anomalies.

409 In brief, the development of the cold tongue during boreal summer, the secondary cooling during boreal winter,  
410 and the presence of TIWs in the equatorial Atlantic exert major controls on the surface ocean hydrographic  
411 characteristics and biogeochemistry on intraseasonal to seasonal time scales. We suggest that the combination of  
412 seasonal thermocline upwelling and TIWs was responsible for the observed enhanced chl-a signals indicating  
413 enhanced variability of primary productivity. Therefore, we can examine their impact on particulate matter build  
414 up and export.

#### 415 **4.2 Upwelling events translate into size-differentiated enhanced export from the mixed layer**

416 The timing of the two upwelling events which lead to chl-a accumulation is consistent with the objective detection  
417 of two peaks in the MaP concentration. Both MiP and MaP in top 100 m are correlated to the in situ chl-a biomass  
418 suggesting that the primary producers provided the elemental particles for the two size classes of marine snow  
419 aggregates. Stronger correlation with MiP than with MaP may indicate that MaP are formed with a delay through  
420 the transformation of MiP by aggregation. This is also supported by Lagrangian chl-a which is more correlated



421 with MiP and MaP (for the same advective time scale of 10 to 15 days) than with concomitant in situ chl-a biomass.  
422 This time scale is consistent with particle aggregation by coagulation of phytoplankton cells followed by the export  
423 of aggregates (Burd & Jackson, 2009; Jackson, 1990). Correlation between Lagrangian chl-a and MiP emphasizes  
424 that MiP are also built up with time.

425 More comprehensive understanding of pelagic functioning can arise from the identification of marine snow  
426 morphotypes (Trudnowska et al., 2021). Fiber Particles (FP), Small Dense particles (SDP), and Small Porous  
427 Particles (SPP) in the epipelagial were significantly correlated with chl-a while no significant correlation was  
428 observed for BDP and BPP. This means that both fiber and porous aggregates might be of phytoplanktonic origin.  
429 Elongated or porous particles in the surface layer, for example, can result from phytoplankton colonies such as  
430 diatom chains or *Trichodesmium* colonies (Dupouy et al., 2018; Villareal et al., 2011) (Fig. S10). These diatoms  
431 were mostly detected during event 1 in our study, their presence increases in conditions of high export systems  
432 (Henson et al., 2019). Porous aggregates might be associated with the accumulation of phytoplankton biomass.  
433 When the bloom is massive enough to enhance aggregation, small porous aggregates are precursors of bigger ones.  
434 As for dense particles, they could be potential fecal pellets produced by zooplankton's feeding as generally found  
435 in other studies (Stemmann & Boss, 2012; Trudnowska et al., 2021).

436 All morphotypes, particle size classes and POC flux were significantly correlated with Lagrangian vorticity and  
437 divergence highlighting that physical dynamics of the upper ocean (such as up- and downwelling) leading to  
438 primary production were the primary control in particle production and transformations. In their paper, Siegel et  
439 al. (2024) found that turbulence levels close to the surface tend to favor smaller particle sizes and increase  
440 fragmentation while turbulence near the base of the mixed layer encourages coagulation and the formation of larger  
441 particles.

442 POC production is associated with phytoplankton production which ultimately influences the export flux. To  
443 investigate the ratio of POC flux leaving the euphotic zone, we calculated the export efficiency ratio at 100 m  
444 during and outside of the events. The export efficiency (e-ratio) was 6-7% and fell within the global average e-ratio  
445 range (Bam et al., 2023 and references within). These values suggest that strong remineralization occurs in surface  
446 waters, aligning with existing literature (Clements et al., 2022). The same e-ratio during and outside of events  
447 highlights the stability of the export efficiency of the equatorial system. One of the hypotheses explaining this  
448 stability is the distribution and contribution of the morphotypes during and outside of export events. During and  
449 before export events, all five morphotypes were detected, with proportions varying with depth. This suggests that  
450 within our observation period, the equatorial region, during or before export events, possesses a similar  
451 phytoplanktonic bloom behavior leading to the same marine snow morphotypes which might explain the similar  
452 behavior of the biological pump. This is in contrast with what was observed for the Arctic system, where two  
453 successive blooms of different nature occur and are associated with different morphotypes. The first bloom was an  
454 ice edge bloom and was dominated by diatoms, while the second was ice free and was associated with the presence  
455 of *Phaeocystis* leading to agglomerated morphotypes and their slow settling compared to the first bloom  
456 (Trudnowska et al., 2021).

457 Another hypothesis for the stability of the system might be related to the tight coupling between primary production  
458 and export. In this study, the lag between PP and particle production was estimated to be 10-15 days, corresponding





459 to a similarly short lag determined by Henson et al. (2015) usually found in upwelling regions. This lag increases  
460 with the increase of seasonality and also affects the seasonality of the  $e_{\text{eff}}$  (Henson et al., 2015). In our case, the  
461 same  $e_{\text{eff}}$  highlights the low seasonality of the carbon pump in the equatorial system: producers and grazers are  
462 tightly coupled due to the low seasonality in PP and export (Owens et al., 2015). This coupling might be due to the  
463 combination of euphotic-zone irradiance and the supply of nutrients: strong light penetration combined with the  
464 energetic intraseasonal variability of the system bringing nutrients to the surface (Menkes et al., 2002), allows  
465 producers to be present all year long in the surface layer. Further studies on the dynamics and composition of  
466 detrital particles in bloom situations, in combination with planktonic measurements, are necessary to understand  
467 surface dynamics of particle formation and export.

#### 468 **4.3 Deep particle sequestration is driven by compact particles**

469 Particle production within the upper 100 m led to the formation of sinking plumes reaching down to 2000 m of  
470 depth. Although particle concentrations were higher during export events, the vertical carbon flux, within and  
471 outside the plumes followed the general asymptotic shape characteristic of particle flux observations, with rapid  
472 attenuation in the surface layer transitioning to a more gradual decrease in the bathypelagic layer. This was also  
473 true for the MiP and MaP abundances. More likely, the observed general decrease in small and big particles is  
474 driven by biological processes such as degradation and aggregation. Yool et al. (2013), using a biogeochemical  
475 model, attributed the flux of particles at deep depths of the ocean to MaPs. However, Kiko et al. (2017) found an  
476 abundance of MiPs in the bathypelagic zone that can be observed down to the sea floor. They suggest that shedding  
477 and other disaggregation processes might result in a more effective export of particulate matter, both actively and  
478 passively. We suggest that their presence in the meso- and bathypelagic layer highlights both their important roles  
479 in contributing to the flux. The difference in flux amplitude inside versus outside of the plumes, along with the  
480 higher particle concentration within the plumes, suggests a seasonal pulse in flux to the deep sea, as previously  
481 described by Beaulieu (2002). This rapid and deep flux is mainly associated with bloom events, consistent with  
482 earlier observations of flux events reaching depths of up to 4000 m (Beaulieu, 2002; Kiko et al., 2017; Lampitt et  
483 al., 1993).

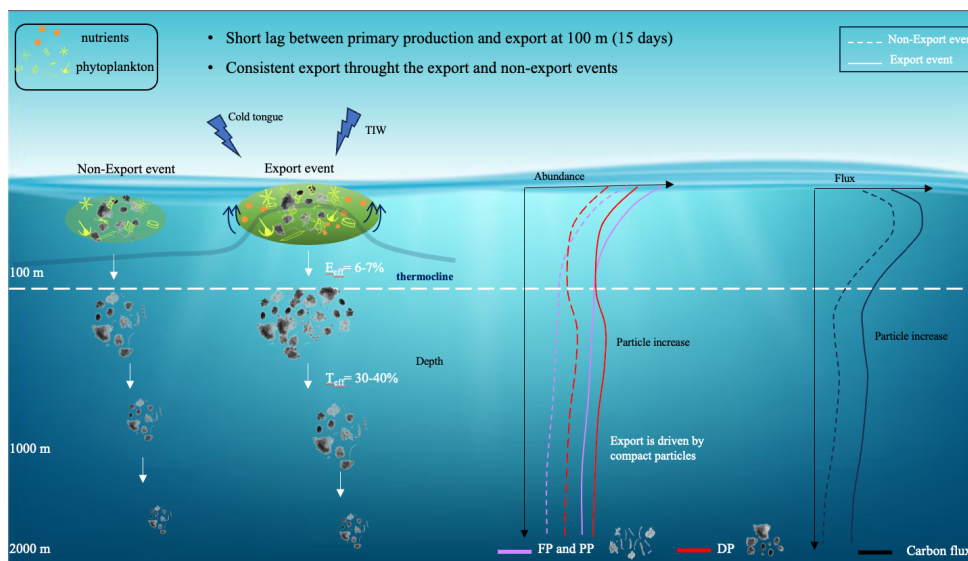
484 We combined the quantitative analysis of particle mass distribution with particle image analysis to investigate the  
485 nature of particles exported to deeper layers. In this study, SDP were more deeply exported compared to other  
486 morphotypes, indicating that most of the MaP abundance found at depth is dominated by small dense particles.  
487 This trend toward more circular and less elongated aggregates with increasing depth confirms prior research  
488 (Drago, 2023; Trudnowska et al., 2021; Accardo et al., submitted). SDP vertical profiles also showed a particle  
489 maximum between 450 and 800 m as found by Kiko et al. (2017) and Siegel et al. (2024), unlike the rest of the  
490 morphotypes which attenuated with depth. The observed increase in small particles is more likely driven by diel  
491 vertical migrations of zooplankton that actively exports organic material to depth (Hidaka et al., 2001; Turner,  
492 2015). This can be confirmed by the increase of zooplankton for all periods between 300-600 m (Fig. S11)  
493 coinciding with the depth of increase of dense particles and the upper limit of zooplankton migration depth  
494 extracted from shipboard ADCP data (shown in Fig. S11) and the range mentioned in Kiko et al., (2017) and  
495 Bianchi & Mislán, (2016). Kiko et al. (2017) also found a particle maximum between 300 and 600 m in the  
496 equatorial Atlantic and attributed it to migrating zooplankton. Food ingested near the surface is carried downward  
497 in the guts of migrating zooplankton to be egested, eaten by consumers of zooplankton, or metabolized at depth



498 (Packard & Gómez, 2013). Model studies suggest that zooplankton diel vertical migration might account for 10-  
499 30% of the total vertical flux of carbon downward from epipelagic layers (Bianchi et al., 2013), enhancing the  
500 efficiency of carbon export (Gorgues et al., 2019) through the generation of fecal pellets which can be incorporated  
501 in marine snow. Kiko et al. (2020) found that gut flux and mortality might make up about 30-40% of particulate  
502 matter supply to the 300-600 m depth layer in the eastern tropical North Atlantic and that the amount of carbon  
503 supplied via these mechanisms could suffice to generate a flux and particle increase.

504 Because our study includes periods of both high and low export, we aimed to assess the flux attenuation rate by  
505 calculating the transfer efficiency for different periods. The transfer efficiency was estimated using flux at depths  
506 of 100 m and 1000 m. Although our export reached depths of 2000 m, we selected the 1000 m layer due to the  
507 relatively small reduction in POC flux with increasing depth, as noted by Francois et al. (2002).  $T_{eff}$  values obtained  
508 in our study indicate a high efficiency of the biological pump with up to 40% of the organic material exported at  
509 100 m also reaching 1000 m, regardless of the conditions. This means that despite seasonal variation in primary  
510 production and carbon flux during and outside of export events, the biological pump exhibits a consistent response  
511 in the equatorial region, rendering it a predictable system. The  $b$  values calculated (around 0.5) show a low  
512 attenuation rate of the computed POC flux, suggesting that part of the particulate matter exported at the equator  
513 and undergoes little further remineralization at mesopelagic depths (Henson et al., 2015; Omand et al., 2015).  
514 Global studies showcased the seasonal and regional variability in the exponent  $b$  and showed values around 0.7 in  
515 Guidi et al, (2015) and 0.6 in Henson et al., (2012) for the tropical equatorial region. The consistent low  $e$ -ratio  
516 associated with high  $T_{eff}$  aligns with the pattern proposed by Guidi et al, (2015) and Henson et al., (2012). This  
517 means that deeper particle injection and rapid sinking result in longer carbon sequestration as the time a given water  
518 parcel needs to travel from the ocean interior to the surface increases with depth.

519 For the first time, we characterized the distribution of particles within an export plume, and offered a morphological  
520 description of exported particles using in situ imaging. The comparisons made with previous studies for the  $e$ -ratio  
521 and the transfer efficiency show that opting for the plume method yields more accurate results and a more  
522 comprehensive understanding of the fate of particles along their progression into deeper layers (Table S1).



523

524 **Figure 6: Illustrative example of the particle export system in the Atlantic equatorial region during export and**  
 525 **non-export events. FP: fiber particles, PP: porous particles, DP: dense particles. Teff: Transfer efficiency, Eeff: Export**  
 526 **efficiency, TIW: Tropical instability Wave.**

527 **5 Conclusion**

528 The integration of the UVP on an Argo float has allowed us to study the temporal variability and the dynamics of  
 529 the BCP. Our study follows the particle dynamics along the water column in the equatorial Atlantic region between  
 530 July 2021 and March 2022 including the strong 2021 Atlantic Niño event, using the plume method and a novel  
 531 BGC-Argo/UVP6 dataset. Ocean dynamics in the equatorial system exhibit a seasonal cycle with a decrease in  
 532 temperature during boreal summer and winter leading to the presence of two distinct blooms. These blooms are  
 533 characterized by significant export events reaching depths of 2000 m. The production and export of carbon during  
 534 that year was dampened because of the strong Atlantic Niño event during boreal summer 2021. Detritus were  
 535 classified into five distinct morphotypes based on morphological variables. In surface waters, marine snow is  
 536 dominated by porous aggregates and fibers while deeper layers primarily receive big and small dense particles  
 537 during export events. Unlike most of the morphotypes decreasing with depth, dense particles show an increase  
 538 between 300-600 m. Zooplankton diel vertical migration might play a role in the generation of a particle maximum  
 539 at intermediate layers consisting of the small dense cluster. The equatorial region acts as a stable export system  
 540 throughout all periods observed, with an export efficiency steadily ranging between 6-7% probably due to the short  
 541 lag between the primary production and the export and the same morphotype composition along the year.  
 542 Regardless of the initial conditions, 30-40% of the flux at 100 m is exported to 1000 m. Such consistency highlights  
 543 the equilibrium inherent in the equatorial region's carbon dynamics along the float trajectory during this special  
 544 event, providing further context to the observed patterns of carbon and particle export. Moreover, it underscores  
 545 the necessity for additional observations to ascertain whether the system is truly stable over the long term. This  
 546 study contributes to a deeper understanding of the intricacies of carbon cycling in equatorial waters using  
 547 autonomous vehicle-derived estimates of particle fluxes. By elucidating the role of export events and different  
 548 particle morphotypes, we underscore the significance of these factors in shaping the equatorial biological pump.



549 The successful combination of the UVP6 with other float sensors and the development of a continuous monitoring  
550 strategy will provide insights that were previously unattainable with sparse and temporally limited shipboard and  
551 moored sediment trap observations.

#### 552 **6 Code availability**

553 The codes used post-data treatment are available upon request to the lead author.

#### 554 **7 Data availability**

555 The sea surface temperature data is available on the NOAA website at:  
556 <https://psl.noaa.gov/data/gridded/data.noaa.oisst.v2.highres.htm>. Float data are available at <https://argo.ucsd.edu>.  
557 Data used in this manuscript for the carbon flux and particle concentrations are available online using the following  
558 DOI: 10.5281/zenodo.14007570. Further data can be made available by the authors upon request.

#### 559 **8 Author contribution**

560 JH, RK, and LS developed the study's concept. RK, LS, JH, FPT, PB, and AB contributed to data acquisition; RK,  
561 LS, JH, PB, AA, AB, and FPT contributed substantially to the data analysis; JH wrote the initial version of the  
562 paper. All authors contributed substantially to drafting the manuscript; All authors approved the final submitted  
563 manuscript.

#### 564 **9 Competing interests**

565 The authors declare that they have no conflict of interest.

#### 566 **9 Acknowledgments**

567 The study was supported by EU H2020 under grant agreement 817578 TRIATLAS project. RK acknowledges  
568 support via a Make Our Planet Great Again grant from the French National Research Agency (ANR) within the  
569 Programme d'Investissements d'Avenir #ANR-19-MPGA-0012 and funding from the Heisenberg Programme of  
570 the German Science Foundation #KI 1387/5-1. We thank the crews, scientists, and technicians involved in the  
571 deployment and recovery of the Argo float during RV *Sonne* cruise SO284 and PIRATA FR32 cruise with RV  
572 *Thalassa*.

#### 573 **10 References**

- 574 Alldredge, A. L. and Silver, M. W.: Characteristics, dynamics and significance of marine snow, *Prog. Oceanogr.*,  
575 20, 41–82, [https://doi.org/10.1016/0079-6611\(88\)90053-5](https://doi.org/10.1016/0079-6611(88)90053-5), 1988.
- 576 Athie, G. and Marin, F.: Cross-equatorial structure and temporal modulation of intraseasonal variability at the  
577 surface of the Tropical Atlantic Ocean, *J. Geophys. Res.*, 113, C08020, <https://doi.org/10.1029/2007JC004332>,  
578 2008.
- 579 Bach, L. T., Stange, P., Taucher, J., Achterberg, E. P., Algueró-Muñiz, M., Horn, H., Esposito, M., and Riebesell,  
580 U.: The Influence of Plankton Community Structure on Sinking Velocity and Remineralization Rate of Marine  
581 Aggregates, *Glob. Biogeochem. Cycles*, 33, 971–994, <https://doi.org/10.1029/2019GB006256>, 2019.
- 582 Bam, W., Gasser, B., Maiti, K., Levy, I., Miquel, J. C., Hansman, R. L., Scholten, J., Xie, R. C., Sommer, S., Kiko,



- 583 R., and Swarzenski, P. W.: Particulate organic carbon export fluxes estimates by  $^{234}\text{Th}/^{238}\text{U}$  disequilibrium in the  
584 oxygen minimum zone off the Peruvian coast, *Mar. Chem.*, 257, 104325,  
585 <https://doi.org/10.1016/j.marchem.2023.104325>, 2023.
- 586 Baudena, A., Ser-Giacomi, E., D’Onofrio, D., Capet, X., Cotté, C., Cherel, Y., and D’Ovidio, F.: Fine-scale  
587 structures as spots of increased fish concentration in the open ocean, *Sci. Rep.*, 11, 15805,  
588 <https://doi.org/10.1038/s41598-021-94368-1>, 2021.
- 589 Beaulieu, S. E.: Accumulation and fate of phytodetritus on the sea floor, 2002.
- 590 Bernardello, R., Marinov, I., Palter, J. B., Sarmiento, J. L., Galbraith, E. D., and Slater, R. D.: Response of the  
591 Ocean Natural Carbon Storage to Projected Twenty-First-Century Climate Change, *J. Clim.*, 27, 2033–2053,  
592 <https://doi.org/10.1175/JCLI-D-13-00343.1>, 2014.
- 593 Bianchi, D. and Mislan, K. a. S.: Global patterns of diel vertical migration times and velocities from acoustic data,  
594 *Limnol. Oceanogr.*, 61, 353–364, <https://doi.org/10.1002/lno.10219>, 2016.
- 595 Bianchi, D., Galbraith, E. D., Carozza, D. A., Mislan, K. A. S., and Stock, C. A.: Intensification of open-ocean  
596 oxygen depletion by vertically migrating animals, *Nat. Geosci.*, 6, 545–548, <https://doi.org/10.1038/ngeo1837>,  
597 2013.
- 598 Bianchi, D., Weber, T. S., Kiko, R., and Deutsch, C.: Global niche of marine anaerobic metabolisms expanded by  
599 particle microenvironments, *Nat. Geosci.*, 11, 263–268, <https://doi.org/10.1038/s41561-018-0081-0>, 2018.
- 600 Biddanda, B. and Pomeroy, L.: Microbial aggregation and degradation of phytoplankton-derived detritus in  
601 seawater. I. Microbial succession, *Mar. Ecol. Prog. Ser.*, 42, 79–88, <https://doi.org/10.3354/meps042079>, 1988.
- 602 Bopp, L., Resplandy, L., Orr, J. C., Doney, S. C., Dunne, J. P., Gehlen, M., Halloran, P., Heinze, C., Ilyina, T.,  
603 Séférian, R., Tjiputra, J., and Vichi, M.: Multiple stressors of ocean ecosystems in the 21st century: projections  
604 with CMIP5 models, *Biogeosciences*, 10, 6225–6245, <https://doi.org/10.5194/bg-10-6225-2013>, 2013.
- 605 Boyd, P. W., Claustre, H., Levy, M., Siegel, D. A., and Weber, T.: Multi-faceted particle pumps drive carbon  
606 sequestration in the ocean, *Nature*, 568, 327–335, <https://doi.org/10.1038/s41586-019-1098-2>, 2019.
- 607 Brandt, P., Caniaux, G., Bourlès, B., Lazar, A., Dengler, M., Funk, A., Hormann, V., Giordani, H., and Marin, F.:  
608 Equatorial upper-ocean dynamics and their interaction with the West African monsoon, *Atmospheric Sci. Lett.*, 12,  
609 24–30, <https://doi.org/10.1002/asl.287>, 2011.
- 610 Brandt, P., Alory, G., Awo, F. M., Dengler, M., Djakouré, S., Imbol Koungue, R. A., Jouanno, J., Körner, M.,  
611 Roch, M., and Rouault, M.: Physical processes and biological productivity in the upwelling regions of the tropical  
612 Atlantic, *Ocean Sci.*, 19, 581–601, <https://doi.org/10.5194/os-19-581-2023>, 2023.
- 613 Briggs, N., Perry, M. J., Cetinić, I., Lee, C., D’Asaro, E., Gray, A. M., and Rehm, E.: High-resolution observations  
614 of aggregate flux during a sub-polar North Atlantic spring bloom, *Deep Sea Res. Part Oceanogr. Res. Pap.*, 58,  
615 1031–1039, <https://doi.org/10.1016/j.dsr.2011.07.007>, 2011.
- 616 Briggs, N., Dall’Olmo, G., and Claustre, H.: Major role of particle fragmentation in regulating biological  
617 sequestration of  $\text{CO}_2$  by the oceans, *Science*, 367, 791–793, <https://doi.org/10.1126/science.aay1790>, 2020.
- 618 Buesseler, K. O., Lamborg, C. H., Boyd, P. W., Lam, P. J., Trull, T. W., Bidigare, R. R., Bishop, J. K. B., Casciotti,  
619 K. L., Dehairs, F., Elskens, M., Honda, M., Karl, D. M., Siegel, D. A., Silver, M. W., Steinberg, D. K., Valdes, J.,  
620 Van Mooy, B., and Wilson, S.: Revisiting Carbon Flux Through the Ocean’s Twilight Zone, *Science*, 316, 567–  
621 570, <https://doi.org/10.1126/science.1137959>, 2007.
- 622 Buesseler, K. O., Boyd, P. W., Black, E. E., and Siegel, D. A.: Metrics that matter for assessing the ocean biological



- 623 carbon pump, *Proc. Natl. Acad. Sci.*, 117, 9679–9687, <https://doi.org/10.1073/pnas.1918114117>, 2020.
- 624 Burd, A. B. and Jackson, G. A.: Particle Aggregation, *Annu. Rev. Mar. Sci.*, 1, 65–90,  
625 <https://doi.org/10.1146/annurev.marine.010908.163904>, 2009.
- 626 Cael, B. B., Cavan, E. L., and Britten, G. L.: Reconciling the Size-Dependence of Marine Particle Sinking Speed,  
627 *Geophys. Res. Lett.*, 48, e2020GL091771, <https://doi.org/10.1029/2020GL091771>, 2021.
- 628 Claustre, H., Johnson, K. S., and Takeshita, Y.: Observing the Global Ocean with Biogeochemical-Argo, *Annu.*  
629 *Rev. Mar. Sci.*, 12, 23–48, <https://doi.org/10.1146/annurev-marine-010419-010956>, 2020.
- 630 Clements, D. J., Yang, S., Weber, T., McDonnell, A. M. P., Kiko, R., Stemann, L., and Bianchi, D.: Constraining  
631 the Particle Size Distribution of Large Marine Particles in the Global Ocean With *In Situ* Optical Observations and  
632 Supervised Learning, *Glob. Biogeochem. Cycles*, 36, e2021GB007276, <https://doi.org/10.1029/2021GB007276>,  
633 2022.
- 634 Clements, D. J., Yang, S., Weber, T., McDonnell, A. M. P., Kiko, R., Stemann, L., and Bianchi, D.: New Estimate  
635 of Organic Carbon Export From Optical Measurements Reveals the Role of Particle Size Distribution and Export  
636 Horizon, *Glob. Biogeochem. Cycles*, 37, e2022GB007633, <https://doi.org/10.1029/2022GB007633>, 2023.
- 637 De Boyer Montégut, C., Madec, G., Fischer, A. S., Lazar, A., and Iudicone, D.: Mixed layer depth over the global  
638 ocean: An examination of profile data and a profile-based climatology, *J. Geophys. Res. Oceans*, 109,  
639 2004JC002378, <https://doi.org/10.1029/2004JC002378>, 2004.
- 640 De La Rocha, C. L.: *The biological pump*, Elsevier, Amsterdam Heidelberg, 2004.
- 641 DeVries, T., Primeau, F., and Deutsch, C.: The sequestration efficiency of the biological pump, *Geophys. Res.*  
642 *Lett.*, 39, 2012GL051963, <https://doi.org/10.1029/2012GL051963>, 2012.
- 643 Dilling, L. and Alldredge, A. L.: Fragmentation of marine snow by swimming macrozooplankton: A new process  
644 impacting carbon cycling in the sea, *Deep Sea Res. Part Oceanogr. Res. Pap.*, 47, 1227–1245,  
645 [https://doi.org/10.1016/S0967-0637\(99\)00105-3](https://doi.org/10.1016/S0967-0637(99)00105-3), 2000.
- 646 Dupouy, C., Frouin, R., Tedetti, M., Maillard, M., Rodier, M., Lombard, F., Guidi, L., Picheral, M., Neveux, J.,  
647 Duhamel, S., Charrière, B., and Sempéré, R.: Diazotrophic *Trichodesmium* impact on UV–Vis radiance and  
648 pigment composition in the western tropical South Pacific, *Biogeosciences*, 15, 5249–5269,  
649 <https://doi.org/10.5194/bg-15-5249-2018>, 2018.
- 650 Engel, A., Cisternas-Novoa, C., Hauss, H., Kiko, R., and Le Moigne, F. A. C.: Hypoxia-tolerant zooplankton may  
651 reduce biological carbon pump efficiency in the Humboldt current system off Peru, *Commun. Earth Environ.*, 4,  
652 458, <https://doi.org/10.1038/s43247-023-01140-6>, 2023.
- 653 Fabri-Ruiz, S., Baudena, A., Moullec, F., Lombard, F., Irisson, J.-O., and Pedrotti, M. L.: Mistaking plastic for  
654 zooplankton: Risk assessment of plastic ingestion in the Mediterranean sea, *Sci. Total Environ.*, 856, 159011,  
655 <https://doi.org/10.1016/j.scitotenv.2022.159011>, 2023.
- 656 Fischer, G., Ratmeyer, V., and Wefer, G.: Organic carbon fluxes in the Atlantic and the Southern Ocean:  
657 relationship to primary production compiled from satellite radiometer data, 2000.
- 658 Foltz, G. R., Hummels, R., Dengler, M., Perez, R. C., and Araujo, M.: Vertical Turbulent Cooling of the Mixed  
659 Layer in the Atlantic ITCZ and Trade Wind Regions, *J. Geophys. Res. Oceans*, 125, e2019JC015529,  
660 <https://doi.org/10.1029/2019JC015529>, 2020.
- 661 Forest, A., Babin, M., Stemann, L., Picheral, M., Sampei, M., Fortier, L., Gratton, Y., Bélanger, S., Devred, E.,  
662 Sahlin, J., Doxaran, D., Joux, F., Ortega-Retuerta, E., Martín, J., Jeffrey, W. H., Gasser, B., and Carlos Miquel, J.:



- 663 Ecosystem function and particle flux dynamics across the Mackenzie Shelf (Beaufort Sea, Arctic Ocean): an  
664 integrative analysis of spatial variability and biophysical forcings, *Biogeosciences*, 10, 2833–2866,  
665 <https://doi.org/10.5194/bg-10-2833-2013>, 2013.
- 666 Fox, J. E., Behrenfeld, M., Halsey, K. H., and Graff, J.: Global estimates of particulate organic carbon from the  
667 surface ocean to the base of the mesopelagic, <https://doi.org/10.22541/essoar.171017314.40658424/v1>, 11 March  
668 2024.
- 669 Giering, S. L. C., Sanders, R., Lampitt, R. S., Anderson, T. R., Tamburini, C., Boutrif, M., Zubkov, M. V., Marsay,  
670 C. M., Henson, S. A., Saw, K., Cook, K., and Mayor, D. J.: Reconciliation of the carbon budget in the ocean's  
671 twilight zone, *Nature*, 507, 480–483, <https://doi.org/10.1038/nature13123>, 2014.
- 672 Gorgues, T., Aumont, O., and Memery, L.: Simulated Changes in the Particulate Carbon Export Efficiency due to  
673 Diel Vertical Migration of Zooplankton in the North Atlantic, *Geophys. Res. Lett.*, 46, 5387–5395,  
674 <https://doi.org/10.1029/2018GL081748>, 2019.
- 675 Grodsky, S. A., Carton, J. A., and McClain, C. R.: Variability of upwelling and chlorophyll in the equatorial  
676 Atlantic, *Geophys. Res. Lett.*, 35, L03610, <https://doi.org/10.1029/2007GL032466>, 2008.
- 677 Guidi, L., Jackson, G. A., Stemmann, L., Miquel, J. C., Picheral, M., and Gorsky, G.: Relationship between particle  
678 size distribution and flux in the mesopelagic zone, *Deep Sea Res. Part Oceanogr. Res. Pap.*, 55, 1364–1374,  
679 <https://doi.org/10.1016/j.dsr.2008.05.014>, 2008.
- 680 Guidi, L., Stemmann, L., Jackson, G. A., Ibanez, F., Claustre, H., Legendre, L., Picheral, M., and Gorsky, G.:  
681 Effects of phytoplankton community on production, size, and export of large aggregates: A world-ocean analysis,  
682 *Limnol. Oceanogr.*, 54, 1951–1963, <https://doi.org/10.4319/lo.2009.54.6.1951>, 2009.
- 683 Guidi, L., Legendre, L., Reygondeau, G., Uitz, J., Stemmann, L., and Henson, S. A.: A new look at ocean carbon  
684 remineralization for estimating deepwater sequestration, *Glob. Biogeochem. Cycles*, 29, 1044–1059,  
685 <https://doi.org/10.1002/2014GB005063>, 2015.
- 686 Henson, S., Le Moigne, F., and Giering, S.: Drivers of Carbon Export Efficiency in the Global Ocean, *Glob.*  
687 *Biogeochem. Cycles*, 33, 891–903, <https://doi.org/10.1029/2018GB006158>, 2019.
- 688 Henson, S. A., Yool, A., and Sanders, R.: Variability in efficiency of particulate organic carbon export: A model  
689 study, *Glob. Biogeochem. Cycles*, 29, 33–45, <https://doi.org/10.1002/2014GB004965>, 2015.
- 690 Hernández-Carrasco, I., Orfila, A., Rossi, V., and Garçon, V.: Effect of small scale transport processes on  
691 phytoplankton distribution in coastal seas, *Sci. Rep.*, 8, 8613, <https://doi.org/10.1038/s41598-018-26857-9>, 2018.
- 692 Heukamp, F. O., Brandt, P., Dengler, M., Tuchen, F. P., McPhaden, M. J., and Moum, J. N.: Tropical Instability  
693 Waves and Wind-Forced Cross-Equatorial Flow in the Central Atlantic Ocean, *Geophys. Res. Lett.*, 49,  
694 e2022GL099325, <https://doi.org/10.1029/2022GL099325>, 2022.
- 695 Hidaka, K., Kawaguchi, K., Murakami, M., and Takahashi, M.: Downward transport of organic carbon by diel  
696 migratory micronekton in the western equatorial Pacific: its quantitative and qualitative importance, 2001.
- 697 Huang, B., Liu, C., Banzon, V., Freeman, E., Graham, G., Hankins, B., Smith, T., and Zhang, H.-M.: Improvements  
698 of the Daily Optimum Interpolation Sea Surface Temperature (DOISST) Version 2.1, *J. Clim.*, 34, 2923–2939,  
699 <https://doi.org/10.1175/JCLI-D-20-0166.1>, 2021.
- 700 Hummels, R., Dengler, M., and Bourlès, B.: Seasonal and regional variability of upper ocean diapycnal heat flux  
701 in the Atlantic cold tongue, *Prog. Oceanogr.*, 111, 52–74, <https://doi.org/10.1016/j.pocean.2012.11.001>, 2013.
- 702 Inoue, R., Lien, R., Moum, J. N., Perez, R. C., and Gregg, M. C.: Variations of Equatorial Shear, Stratification, and



- 703 Turbulence Within a Tropical Instability Wave Cycle, *J. Geophys. Res. Oceans*, 124, 1858–1875,  
704 <https://doi.org/10.1029/2018JC014480>, 2019.
- 705 Irigoien, X., Klevjer, T. A., Røstad, A., Martinez, U., Boyra, G., Acuña, J. L., Bode, A., Echevarria, F., Gonzalez-  
706 Gordillo, J. I., Hernandez-Leon, S., Agusti, S., Aksnes, D. L., Duarte, C. M., and Kaartvedt, S.: Large mesopelagic  
707 fishes biomass and trophic efficiency in the open ocean, *Nat. Commun.*, 5, 3271,  
708 <https://doi.org/10.1038/ncomms4271>, 2014.
- 709 Jackson, G. A.: A model of the formation of marine algal flocs by physical coagulation processes, *Deep Sea Res.*  
710 *Part Oceanogr. Res. Pap.*, 37, 1197–1211, [https://doi.org/10.1016/0198-0149\(90\)90038-W](https://doi.org/10.1016/0198-0149(90)90038-W), 1990.
- 711 Jouanno, J., Marin, F., Du Penhoat, Y., Sheinbaum, J., and Molines, J.-M.: Seasonal heat balance in the upper 100  
712 m of the equatorial Atlantic Ocean, *J. Geophys. Res.*, 116, C09003, <https://doi.org/10.1029/2010JC006912>, 2011.
- 713 Kiko, R., Biastoch, A., Brandt, P., Cravatte, S., Hauss, H., Hummels, R., Kriest, I., Marin, F., McDonnell, A. M.  
714 P., Oschlies, A., Picheral, M., Schwarzkopf, F. U., Thurnherr, A. M., and Stemmann, L.: Biological and physical  
715 influences on marine snowfall at the equator, *Nat. Geosci.*, 10, 852–858, <https://doi.org/10.1038/ngeo3042>, 2017.
- 716 Kiko, R., Brandt, P., Christiansen, S., Faustmann, J., Kriest, I., Rodrigues, E., Schütte, F., and Hauss, H.:  
717 Zooplankton-Mediated Fluxes in the Eastern Tropical North Atlantic, *Front. Mar. Sci.*, 7, 358,  
718 <https://doi.org/10.3389/fmars.2020.00358>, 2020.
- 719 Kiko, R., Picheral, M., Antoine, D., Babin, M., Berline, L., Biard, T., Boss, E., Brandt, P., Carlotti, F., Christiansen,  
720 S., Coppola, L., De La Cruz, L., Diamond-Riquier, E., Durrieu De Madron, X., Elineau, A., Gorsky, G., Guidi, L.,  
721 Hauss, H., Irisson, J.-O., Karp-Boss, L., Karstensen, J., Kim, D., Lekanoff, R. M., Lombard, F., Lopes, R. M.,  
722 Marec, C., McDonnell, A. M. P., Niemeyer, D., Noyon, M., O'Daly, S. H., Ohman, M. D., Pretty, J. L., Rogge, A.,  
723 Searson, S., Shibata, M., Tanaka, Y., Tanhua, T., Taucher, J., Trudnowska, E., Turner, J. S., Waite, A., and  
724 Stemmann, L.: A global marine particle size distribution dataset obtained with the Underwater Vision Profiler 5,  
725 *Earth Syst. Sci. Data*, 14, 4315–4337, <https://doi.org/10.5194/essd-14-4315-2022>, 2022.
- 726 Koestner, D., Stramski, D., and Reynolds, R. A.: A Multivariable Empirical Algorithm for Estimating Particulate  
727 Organic Carbon Concentration in Marine Environments From Optical Backscattering and Chlorophyll-a  
728 Measurements, *Front. Mar. Sci.*, 9, 941950, <https://doi.org/10.3389/fmars.2022.941950>, 2022.
- 729 Kriest, I.: Different parameterizations of marine snow in a 1D-model and their influence on representation of marine  
730 snow, nitrogen budget and sedimentation, *Deep Sea Res. Part Oceanogr. Res. Pap.*, 49, 2133–2162,  
731 [https://doi.org/10.1016/S0967-0637\(02\)00127-9](https://doi.org/10.1016/S0967-0637(02)00127-9), 2002.
- 732 Lampitt, R. S., Wishner, K. F., Turley, C. M., and Angel, M. V.: Marine snow studies in the Northeast Atlantic  
733 Ocean: distribution, composition and role as a food source for migrating plankton, *Mar. Biol.*, 116, 689–702,  
734 <https://doi.org/10.1007/BF00355486>, 1993.
- 735 Lee, S., Lopez, H., Tuchen, F. P., Kim, D., Foltz, G. R., and Wittenberg, A. T.: On the Genesis of the 2021 Atlantic  
736 Niño, *Geophys. Res. Lett.*, 50, e2023GL104452, <https://doi.org/10.1029/2023GL104452>, 2023.
- 737 Longhurst, A.: Seasonal cooling and blooming in tropical oceans, *Deep Sea Res. Part Oceanogr. Res. Pap.*, 40,  
738 2145–2165, [https://doi.org/10.1016/0967-0637\(93\)90095-K](https://doi.org/10.1016/0967-0637(93)90095-K), 1993.
- 739 Loukos, H. and Mémerly, L.: Simulation of the nitrate seasonal cycle in the equatorial Atlantic Ocean during 1983  
740 and 1984, *J. Geophys. Res. Oceans*, 104, 15549–15573, <https://doi.org/10.1029/1999JC900084>, 1999.
- 741 Martin, J. H., Knauer, G. A., Karl, D. M., and Broenkow, W. W.: VERTEX: carbon cycling in the northeast Pacific,  
742 *Deep Sea Res. Part Oceanogr. Res. Pap.*, 34, 267–285, [https://doi.org/10.1016/0198-0149\(87\)90086-0](https://doi.org/10.1016/0198-0149(87)90086-0), 1987.





- 743 Menkes, C. E., Kennan, S., Flament, P., Dandonneau, Y., Masson, S., Biessy, B., Marchal, E., and Eldin, G.: A  
744 whirling ecosystem in the equatorial Atlantic, *Geophys. Res. Lett.*, 29, 1553,  
745 <https://doi.org/10.1029/2001GL014576>, 2002.
- 746 Moore, C. M., Mills, M. M., Arrigo, K. R., Berman-Frank, I., Bopp, L., Boyd, P. W., Galbraith, E. D., Geider, R.  
747 J., Guieu, C., Jaccard, S. L., Jickells, T. D., La Roche, J., Lenton, T. M., Mahowald, N. M., Marañón, E., Marinov,  
748 I., Moore, J. K., Nakatsuka, T., Oschlies, A., Saito, M. A., Thingstad, T. F., Tsuda, A., and Ulloa, O.: Processes  
749 and patterns of oceanic nutrient limitation, *Nat. Geosci.*, 6, 701–710, <https://doi.org/10.1038/ngeo1765>, 2013.
- 750 Moum, J. N., Lien, R.-C., Perlin, A., Nash, J. D., Gregg, M. C., and Wiles, P. J.: Sea surface cooling at the Equator  
751 by subsurface mixing in tropical instability waves, *Nat. Geosci.*, 2, 761–765, <https://doi.org/10.1038/ngeo657>,  
752 2009.
- 753 Okumura, Y. and Xie, S.-P.: Some Overlooked Features of Tropical Atlantic Climate Leading to a New Niño-Like  
754 Phenomenon\*, *J. Clim.*, 19, 5859–5874, <https://doi.org/10.1175/JCLI3928.1>, 2006.
- 755 Olivier, L., Reverdin, G., Hasson, A., and Boutin, J.: Tropical Instability Waves in the Atlantic Ocean: Investigating  
756 the Relative Role of Sea Surface Salinity and Temperature From 2010 to 2018, *J. Geophys. Res. Oceans*, 125,  
757 e2020JC016641, <https://doi.org/10.1029/2020JC016641>, 2020.
- 758 Omand, M. M., D’Asaro, E. A., Lee, C. M., Perry, M. J., Briggs, N., Cetinić, I., and Mahadevan, A.: Eddy-driven  
759 subduction exports particulate organic carbon from the spring bloom, *Science*, 348, 222–225,  
760 <https://doi.org/10.1126/science.1260062>, 2015.
- 761 Owens, S. A., Pike, S., and Buesseler, K. O.: Thorium-234 as a tracer of particle dynamics and upper ocean export  
762 in the Atlantic Ocean, *Deep Sea Res. Part II Top. Stud. Oceanogr.*, 116, 42–59,  
763 <https://doi.org/10.1016/j.dsr2.2014.11.010>, 2015.
- 764 Packard, T. T. and Gómez, M.: Modeling vertical carbon flux from zooplankton respiration, *Prog. Oceanogr.*, 110,  
765 59–68, <https://doi.org/10.1016/j.pocean.2013.01.003>, 2013.
- 766 Picheral, M., Guidi, L., Stemmann, L., Karl, D. M., Iddaoud, G., and Gorsky, G.: The Underwater Vision Profiler  
767 5: An advanced instrument for high spatial resolution studies of particle size spectra and zooplankton, *Limnol.*  
768 *Oceanogr. Methods*, 8, 462–473, <https://doi.org/10.4319/lom.2010.8.462>, 2010.
- 769 Picheral, M., Colin, S., and Irsson, J. O.: EcoTaxa, a tool for the taxonomic classification of images, 2017.
- 770 Picheral, M., Catalano, C., Brousseau, D., Claustre, H., Coppola, L., Leymarie, E., Coindat, J., Dias, F., Fevre, S.,  
771 Guidi, L., Irsson, J. O., Legendre, L., Lombard, F., Mortier, L., Penkerch, C., Rogge, A., Schmechtig, C., Thibault,  
772 S., Tixier, T., Waite, A., and Stemmann, L.: The Underwater Vision Profiler 6: an imaging sensor of particle size  
773 spectra and plankton, for autonomous and cabled platforms, *Limnol. Oceanogr. Methods*, 20, 115–129,  
774 <https://doi.org/10.1002/lom3.10475>, 2022.
- 775 Ploug, H. and Grossart, H.: Bacterial growth and grazing on diatom aggregates: Respiratory carbon turnover as a  
776 function of aggregate size and sinking velocity, *Limnol. Oceanogr.*, 45, 1467–1475,  
777 <https://doi.org/10.4319/lo.2000.45.7.1467>, 2000.
- 778 Radenac, M.-H., Jouanno, J., Tchamabi, C. C., Awo, M., Bourlès, B., Arnault, S., and Aumont, O.: Physical drivers  
779 of the nitrate seasonal variability in the Atlantic cold tongue, *Biogeosciences*, 17, 529–545,  
780 <https://doi.org/10.5194/bg-17-529-2020>, 2020.
- 781 Ramondenc, S., Madeleine, G., Lombard, F., Santinelli, C., Stemmann, L., Gorsky, G., and Guidi, L.: An initial  
782 carbon export assessment in the Mediterranean Sea based on drifting sediment traps and the Underwater Vision



- 783 Profiler data sets, *Deep Sea Res. Part Oceanogr. Res. Pap.*, 117, 107–119,  
784 <https://doi.org/10.1016/j.dsr.2016.08.015>, 2016.
- 785 Rodionov, S. N.: A sequential algorithm for testing climate regime shifts, *Geophys. Res. Lett.*, 31, 2004GL019448,  
786 <https://doi.org/10.1029/2004GL019448>, 2004.
- 787 Rodionov, S. N.: Use of prewhitening in climate regime shift detection, *Geophys. Res. Lett.*, 33, 2006GL025904,  
788 <https://doi.org/10.1029/2006GL025904>, 2006.
- 789 [Schott, F. A., Fischer, J., and Stramma, L.: Transports and Pathways of the Upper-Layer Circulation in the Western](#)  
790 [Tropical Atlantic, \*J. Phys. Oceanogr.\*, 28, 1904–1928, <https://doi.org/10.1175/1520-0485.1998>.](#)
- 791 Ser-Giacomi, E., Baudena, A., Rossi, V., Follows, M., Clayton, S., Vasile, R., López, C., and Hernández-García,  
792 E.: Lagrangian betweenness as a measure of bottlenecks in dynamical systems with oceanographic examples, *Nat.*  
793 *Commun.*, 12, 4935, <https://doi.org/10.1038/s41467-021-25155-9>, 2021.
- 794 Sherman, J., Subramaniam, A., Gorbunov, M. Y., Fernández-Carrera, A., Kiko, R., Brandt, P., and Falkowski, P.  
795 G.: The Photophysiological Response of Nitrogen-Limited Phytoplankton to Episodic Nitrogen Supply Associated  
796 With Tropical Instability Waves in the Equatorial Atlantic, *Front. Mar. Sci.*, 8, 814663,  
797 <https://doi.org/10.3389/fmars.2021.814663>, 2022.
- 798 Shi, W. and Wang, M.: Tropical instability wave modulation of chlorophyll-a in the Equatorial Pacific, *Sci. Rep.*,  
799 11, 22517, <https://doi.org/10.1038/s41598-021-01880-5>, 2021.
- 800 Siegel, D. A., Burd, A. B., Estapa, M., Fields, E., Johnson, L., Romanelli, E., Brzezinski, M. A., Buesseler, K. O.,  
801 Clevenger, S., Cetinić, I., Drago, L., Durkin, C. A., Kiko, R., Kramer, S. J., Maas, A., Omand, M., Passow, U., and  
802 Steinberg, D. K.: 10 Dynamics of Aggregates and Sinking Carbon Fluxes in a 11 Turbulent Ocean 12 Draft: April  
803 22, 2024, n.d.
- 804 Song, Q., Tang, Y., and Aiki, H.: Dual Wave Energy Sources for the Atlantic Niño Events Identified by Wave  
805 Energy Flux in Case Studies, *J. Geophys. Res. Oceans*, 128, e2023JC019972,  
806 <https://doi.org/10.1029/2023JC019972>, 2023.
- 807 Steinberg, D. K. and Landry, M. R.: Zooplankton and the Ocean Carbon Cycle, *Annu. Rev. Mar. Sci.*, 9, 413–444,  
808 <https://doi.org/10.1146/annurev-marine-010814-015924>, 2017.
- 809 Stemann, L. and Boss, E.: Plankton and Particle Size and Packaging: From Determining Optical Properties to  
810 Driving the Biological Pump, *Annu. Rev. Mar. Sci.*, 4, 263–290, [https://doi.org/10.1146/annurev-marine-120710-](https://doi.org/10.1146/annurev-marine-120710-100853)  
811 [100853](https://doi.org/10.1146/annurev-marine-120710-100853), 2012.
- 812 Stemann, L., Gorsky, G., Marty, J.-C., Picheral, M., and Miquel, J.-C.: Four-year study of large-particle vertical  
813 distribution (0–1000m) in the NW Mediterranean in relation to hydrology, phytoplankton, and vertical flux, *Deep*  
814 *Sea Res. Part II Top. Stud. Oceanogr.*, 49, 2143–2162, [https://doi.org/10.1016/S0967-0645\(02\)00032-2](https://doi.org/10.1016/S0967-0645(02)00032-2), 2002.
- 815 Stemann, L., Jackson, G. A., and Ianson, D.: A vertical model of particle size distributions and fluxes in the  
816 midwater column that includes biological and physical processes—Part I: model formulation, *Deep Sea Res. Part*  
817 *Oceanogr. Res. Pap.*, 51, 865–884, <https://doi.org/10.1016/j.dsr.2004.03.001>, 2004a.
- 818 Stemann, L., Jackson, G. A., and Gorsky, G.: A vertical model of particle size distributions and fluxes in the  
819 midwater column that includes biological and physical processes—Part II: application to a three year survey in the  
820 NW Mediterranean Sea, *Deep Sea Res. Part Oceanogr. Res. Pap.*, 51, 885–908,  
821 <https://doi.org/10.1016/j.dsr.2004.03.002>, 2004b.
- 822 Tréguer, P., Bowler, C., Moriceau, B., Dutkiewicz, S., Gehlen, M., Aumont, O., Bittner, L., Dugdale, R., Finkel,



- 823 Z., Iudicone, D., Jahn, O., Guidi, L., Lasbleiz, M., Leblanc, K., Levy, M., and Pondaven, P.: Influence of diatom  
824 diversity on the ocean biological carbon pump, *Nat. Geosci.*, 11, 27–37, <https://doi.org/10.1038/s41561-017-0028->  
825 x, 2018.
- 826 Trudnowska, E., Lacour, L., Ardyna, M., Rogge, A., Irisson, J. O., Waite, A. M., Babin, M., and Stemmann, L.:  
827 Marine snow morphology illuminates the evolution of phytoplankton blooms and determines their subsequent  
828 vertical export, *Nat. Commun.*, 12, 2816, <https://doi.org/10.1038/s41467-021-22994-4>, 2021.
- 829 Tuchen, F. P., Perez, R. C., Foltz, G. R., Brandt, P., and Lumpkin, R.: Multidecadal Intensification of Atlantic  
830 Tropical Instability Waves, *Geophys. Res. Lett.*, 49, e2022GL101073, <https://doi.org/10.1029/2022GL101073>,  
831 2022.
- 832 Tuchen, F. P., Perez, R. C., Foltz, G. R., Brandt, P., Subramaniam, A., Lee, S., Lumpkin, R., and Hummels, R.:  
833 Modulation of Equatorial Currents and Tropical Instability Waves During the 2021 Atlantic Niño, *J. Geophys. Res.*  
834 *Oceans*, 129, e2023JC020431, <https://doi.org/10.1029/2023JC020431>, 2024.
- 835 Turner, J. T.: Zooplankton fecal pellets, marine snow, phytodetritus and the ocean's biological pump, *Prog.*  
836 *Oceanogr.*, 130, 205–248, <https://doi.org/10.1016/j.pocean.2014.08.005>, 2015.
- 837 Villareal, T. A., Adornato, L., Wilson, C., and Schoenbaechler, C. A.: Summer blooms of diatom-diazotroph  
838 assemblages and surface chlorophyll in the North Pacific gyre: A disconnect, *J. Geophys. Res.*, 116, C03001,  
839 <https://doi.org/10.1029/2010JC006268>, 2011.
- 840 Warner, S. J., Holmes, R. M., M. Hawkins, E. H., S. Hoecker-Martínez, M., Savage, A. C., and Moum, J. N.:  
841 Buoyant Gravity Currents Released from Tropical Instability Waves, *J. Phys. Oceanogr.*, 48, 361–382,  
842 <https://doi.org/10.1175/JPO-D-17-0144.1>, 2018.
- 843 Wefer, G. and Fischer, G.: Seasonal patterns of vertical particle flux in equatorial and coastal upwelling areas of  
844 the eastern Atlantic, *Deep Sea Res. Part Oceanogr. Res. Pap.*, 40, 1613–1645, <https://doi.org/10.1016/0967->  
845 0637(93)90019-Y, 1993.
- 846 Yool, A., Popova, E. E., and Anderson, T. R.: MEDUSA-2.0: an intermediate complexity biogeochemical model  
847 of the marine carbon cycle for climate change and ocean acidification studies, *Geosci. Model Dev.*, 6, 1767–1811,  
848 <https://doi.org/10.5194/gmd-6-1767-2013>, 2013.